

## Vibrational properties of metal phosphorus trichalcogenides from first principles

Hashemi, A.; Komsa, H.-P.; Puska, M.; Krasheninnikov, A. V.;

Originally published:

November 2017

**Journal of Physical Chemistry C 121(2017), 27207-27217**

DOI: <https://doi.org/10.1021/acs.jpcc.7b09634>

Perma-Link to Publication Repository of HZDR:

<https://www.hzdr.de/publications/Publ-26580>

Release of the secondary publication  
on the basis of the German Copyright Law § 38 Section 4.

This document is confidential and is proprietary to the American Chemical Society and its authors. Do not copy or disclose without written permission. If you have received this item in error, notify the sender and delete all copies.

**Vibrational Properties of Metal Phosphorus Trichalcogenides  
from First-Principles Calculations**

Journal:	<i>The Journal of Physical Chemistry</i>
Manuscript ID	jp-2017-09634j.R2
Manuscript Type:	Article
Date Submitted by the Author:	13-Nov-2017
Complete List of Authors:	Hashemi, Arsalan; Aalto University, Department of Applied Physics Komsa, Hannu-Pekka; Aalto University, Department of Applied Physics Puska, Martti; Aalto University, Applied Physics Krasheninnikov, Arkady; Helmholtz-Zentrum Dresden-Rossendorf, Ion Beam Centre

SCHOLARONE™  
Manuscripts

# Vibrational Properties of Metal Phosphorus Trichalcogenides from First-Principles Calculations

Arsalan Hashemi,<sup>\*,†</sup> Hannu-Pekka Komsa,<sup>\*,†</sup> Martti Puska,<sup>†</sup> and Arkady V. Krasheninnikov<sup>†,‡</sup>

*Department of Applied Physics, Aalto University, P.O. Box 11100, 00076 Aalto, Finland, and Helmholtz-Zentrum Dresden-Rossendorf, Institute of Ion Beam Physics and Materials Research, 01328 Dresden, Germany*

E-mail: arsalan.hashemi@aalto.fi; hannu-pekka.komsa@aalto.fi

## Abstract

Two-dimensional (2D) sheets of transition metal phosphorus trichalcogenides (TMPTs) offer unique magnetic and optical properties that can complement those found in other 2D materials. Insights into the structure and properties of these materials can be obtained by a juxtaposition of the experimental and calculated Raman spectra, but there is very little theoretical knowledge of the vibrational properties of TMPTs. Using first-principles calculations, we study mechanical and vibrational properties of a large set of monolayer TMPTs. From the phonon dispersion curves, we assess the dynamical stabilities and general trends on the atomic character of the vibrational modes. We determine Raman active modes from group theory, calculate Raman intensities, and analyze them with the help of the corresponding atomic displacements. We evaluate how the mode frequencies shift in response to a biaxial strain. We also determine elastic properties, which show that these systems are softer than many other layered materials. In addition to

shedding light on the general features of vibrational properties of these materials, our results should also prove useful for interpreting experimental Raman spectra.

## 1 Introduction

In quest of expanding the atlas of attainable physical properties of two-dimensional (2D) materials, the research community has started to revisit “old” van der Waals (vdW) layered structures, from which “new” 2D systems can be exfoliated. In this context, the family of transition metal phosphorus trichalcogenides (TMPTs) with a structural formula of  $MPX_3$ , where  $M = V, Mn, Fe, Co, Ni, Cd, Mg, Zn$ ;  $X = S$  or  $Se$ , has recently started to attract interest, since the bulk TMPTs possess band gaps in a range of 1.3–3.5 eV, wider than those in transition metal dichalcogenides (TMDs), where the gaps does not exceed 2 eV. Besides, TMPTs exhibit magnetic ordering and can be exfoliated into single sheets.<sup>1–6</sup> Contrary to many metal chalcogenides, the constituent chemical elements are largely earth abundant and non-toxic. Moreover, as in the case of many layered materials, electronic and optical properties are sensitive to the number of layers, which opens additional degrees of freedom for engineering the electronic properties of these materials. For

<sup>\*</sup>To whom correspondence should be addressed

<sup>†</sup>Department of Applied Physics, Aalto University, P.O. Box 11100, 00076 Aalto, Finland

<sup>‡</sup>Helmholtz-Zentrum Dresden-Rossendorf, Institute of Ion Beam Physics and Materials Research, 01328 Dresden, Germany

1 example, the observed band gap of bulk NiPS<sub>3</sub>  
2 is equal to 1.6 eV, while the exfoliation into the  
3 bilayer results in an indirect-to-direct band gap  
4 transition<sup>7</sup> with a value of the gap being 2.6 eV.

5 The atomic structure of TMPTs is similar  
6 to that of TMDs in the octahedral phase (T-  
7 phase) for the position of the metal and chalcogen  
8 atoms.<sup>8,9</sup> A difference is that one third of  
9 the metal atoms is replaced by P<sub>2</sub> dimers oriented  
10 normal to the layer, as shown in Figure  
11 1. Each [P<sub>2</sub>X<sub>6</sub>]<sup>-4</sup> unit occupies the centre of  
12 the six closest divalent metal ions M<sup>+2</sup> forming  
13 a hexagonal lattice. In addition to their  
14 role in defining the electronic structure, some  
15 of the metal elements in this family of compounds  
16 are magnetic (Fe, Ni, Mn, and Co). As the metal  
17 atoms form a hexagonal lattice, each with three  
18 neighbors, these structures can exhibit stable  
19 magnetic phases. Experimentally Néel and zigzag  
20 antiferromagnetic phases have been observed with  
21 strong intraplanar and weak interplanar coupling.  
22 In fact, these materials were investigated in the  
23 past as an attractive platform to study 2D magnetism.  
24<sup>10,11</sup> The combination of a large band gap and  
25 magnetism are expected to find applications in  
26 optoelectronics, magneto-optics, and magnetic  
27 storage,<sup>12-14</sup> in addition to the applications often  
28 envisioned for layered materials e.g. in electrochemistry.  
29<sup>15</sup>

30 Although magnetic and electronic properties  
31 of the TMPT materials have been extensively  
32 studied, the vibrational properties of monolayer  
33 MPX<sub>3</sub> have been scarcely investigated up to  
34 now. At the same time, the transition into  
35 magnetic state as a function of temperature can  
36 be observed in Raman spectra.<sup>16</sup> In addition,  
37 Raman spectra can be used to assess, e.g.,  
38 mechanical strain, doping, the number of layers  
39 or concentration of defects in 2D materials.  
40<sup>17-21</sup> Thus the precise microscopic knowledge  
41 of the vibrational properties is important for  
42 analyzing the Raman spectra and the phonon  
43 properties affecting thermal transport.

44 To fill the gaps in the existing knowledge,  
45 in this work we perform first-principles  
46 calculations for the phonon spectra, and Raman  
47 intensities of MgPS<sub>3</sub>, MgPSe<sub>3</sub>, MnPS<sub>3</sub>, MnPSe<sub>3</sub>,  
48 FePS<sub>3</sub>, FePSe<sub>3</sub>, NiPS<sub>3</sub>, NiPSe<sub>3</sub>, ZnPS<sub>3</sub>, ZnPSe<sub>3</sub>,  
49 CdPS<sub>3</sub>, and CdPSe<sub>3</sub> compounds. To analyze

the vibrational modes, we examine the ionic  
displacements and the contributions from different  
elements. We further calculate Raman intensities  
and frequency shifts upon application of biaxial  
strain. We also assess the mechanical properties  
of these systems by evaluating elastic constants.  
With the data obtained for a large set of TMPTs,  
we can extract the trends common for the whole  
family of these materials and compare our results  
to other 2D systems.

## 2 Computational Details

Density functional theory (DFT) calculations  
were performed in the framework of the projector  
augmented wave method using VASP<sup>25</sup> code.  
The plane wave basis set with a kinetic energy  
cutoff of 500 eV was used for all materials.  
Very tight convergence criteria are required in  
the calculation of phonon dispersion curves.  
To this end, the total energies in both geometry  
relaxation and in phonon calculations were  
converged within 10<sup>-7</sup> eV and the forces to  
within 0.1 meV/Å.

The different materials considered in this  
work have different magnetic orders, which can  
require the use of unit cells of different sizes.  
Specifically, Mg, Cd, and Zn compounds are  
nonmagnetic (NM) due to the filling of the *d*-  
shell of metal atoms. For the magnetic structures,  
the experimental results reveal the existence of  
two different models of magnetic moments  
ordering.<sup>6,10,26</sup> MnPX<sub>3</sub> shows a Néel  
antiferromagnetic (AFM) phase. Fe and Ni  
materials display zigzag AFM below the Néel  
temperatures. The determination of magnetic  
models is simplified by the fact that the  
magnetic moments originate almost entirely  
from the *d* electrons of the metals in the  
honeycomb lattice. Both the NM and the Néel  
AFM phases can be described using the  
hexagonal primitive cell containing 10 atoms.  
In the case of zigzag AFM phase, a larger  
tetragonal unit cell with 20 atoms needs to  
be adopted. These are both displayed in  
Figure 1. The 6 × 6 × 1 k-mesh was found  
to be sufficient for the Mg, Mn, Zn, and Cd  
compounds. FePX<sub>3</sub> and NiPX<sub>3</sub> require a  
larger 16 × 9 × 1 k-mesh.

**Table 1: Calculated monolayer and experimental bulk lattice constants  $a$ , layer thicknesses  $d$ , and band gaps  $E_g$ , and ground-state magnetic orders. D/I after band gap value denotes direct/indirect gap. The experimental data is taken from Refs.<sup>6,11,22–24</sup>**

	$a$ (Å)		$d$ (Å)		$E_g$ (eV)		Magnetic GS
	PBE	Expt.	PBE	Expt.	PBE	Expt.	PBE
MgPS <sub>3</sub>	6.10	6.09	3.28	3.26	2.84(D)		NM
MgPSe <sub>3</sub>	6.45	6.40	3.47	3.43	2.03(D)		NM
MnPS <sub>3</sub>	6.05	6.08	3.23	3.21	1.33(I)	3.0	Néel AFM
MnPSe <sub>3</sub>	6.39	6.38	3.34	3.28	0.99(I)	2.5	Néel AFM
FePS <sub>3</sub>	5.86	5.95	3.12	3.19	0.12(I)	1.5	zigzag AFM
FePSe <sub>3</sub>	6.22	6.27	3.29	3.17	0.11(I)	1.3	zigzag AFM
NiPS <sub>3</sub>	5.82	5.81	3.03	3.21	0.70(I)	1.6	zigzag AFM
NiPSe <sub>3</sub>	6.17	6.14	3.13	3.30	0.47(I)		zigzag AFM
ZnPS <sub>3</sub>	6.01	5.97	3.23	3.20	2.14(I)	3.4	NM
ZnPSe <sub>3</sub>	6.36	6.29	3.39	3.28	1.32(I)		NM
CdPS <sub>3</sub>	6.30	6.21	3.41	3.38	1.93(I)	3.5	NM
CdPSe <sub>3</sub>	6.62	6.51	3.58	3.25	1.29(I)		NM

For describing the exchange and correlation effects, we have chosen to adopt the functional proposed by Perdew, Burke, and Ernzerhof (PBE).<sup>27</sup> Calculated lattice parameters and layer thicknesses are compared with the experimental ones in Table 1. The experimental values correspond to the bulk systems. Table 1 also shows the calculated magnetic ground states, which were determined by comparing the total energies for four common magnetic moment orderings<sup>28</sup> and moreover found to agree with the experimental bulk magnetic orderings for all materials. The PBE results are in overall good agreement with the previous theoretical data<sup>4,28</sup> and the experimental values, although there appears to be an overestimation of the lattice constant in the case of CdPX<sub>3</sub> and an underestimation in the case for FePX<sub>3</sub>, as well as underestimation of the layer thickness of NiPX<sub>3</sub>. In addition, the lowest energy configuration of the FePX<sub>3</sub> compounds was accompanied by a strong structural distortion. The two Fe-Fe bond lengths along the zigzag chain became very different, 2.78 Å and 3.74 Å, for FePS<sub>3</sub> and 3.31 Å and 3.82 Å for FePSe<sub>3</sub>, while they should be equal according to the experimentally determined crystal structures.<sup>11,16</sup> The problem may be related to the poor description of strong correlation ef-

fects among  $d$ -orbital electrons in some metals. This could be remedied, e.g., by the  $+U$  correction, but for the sake of consistency and also uncertainties in the choice of  $U$ , we generally refrain from adding  $+U$  corrections, and the results reported for FePX<sub>3</sub> correspond to the (metastable) symmetric structure. This yields Fe-Fe bond lengths of 3.32 Å and 3.52 Å for FePS<sub>3</sub> and FePSe<sub>3</sub>, respectively. A comparison of the vibrational properties between the symmetric and distorted structures are given in the Appendix and discussed in more detail later on. The available experimental data on the band gaps of monolayer TMPTs is very limited. Comparison to bulk band gaps are shown in Table 1 and shows that the calculated values are consistently 1–1.5 eV lower. Quantitative comparison to calculations is hindered by the different number of layers as well as underestimation of band gaps calculated by PBE functional. Nevertheless, we can conclude that all these materials should be semiconductors.

The polarizability tensors for Raman calculations and the elastic constants were determined with the same parameters as above within the framework of the density functional perturbation theory (DFPT).<sup>29</sup> The lattice vibrations and dynamical stabilities were assessed using the PHONOPY code<sup>30</sup> within the supercell ap-

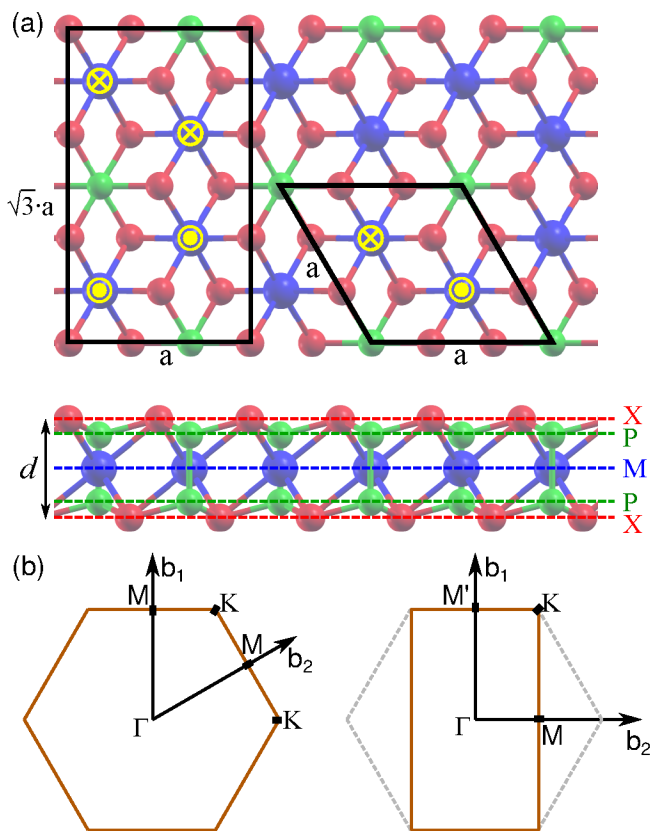


Figure 1: (a) Schematic representation of the atomic structure of the  $MPX_3$  monolayer, the top and side views. Blue, green, and red balls correspond to metal (M), phosphorus (P), and chalcogen (X) atoms, respectively. The rectangular unit cell and the hexagonal primitive cell are shown in the top view panel by black lines. The yellow markers  $\otimes$  and  $\odot$  show the direction of magnetic moments, illustrating the zigzag AFM order in the rectangular unit cell and the Néel AFM order in the primitive cell. The thickness of the sheet is quantified using the parameter  $d$ , which is equal to the distance between chalcogen atoms in a single layer. Note that it is different from the unit cell length  $c$  in the bulk materials. (b) Sketch of the Brillouin zones for the hexagonal and rectangular unit cells, as well as the labeling adopted for the high-symmetry k-points used in the phonon dispersions plots.

proach. Here, we used the finite displacement method instead of DFPT since, according to our calculations it yields a better description of the flexural mode near the  $\Gamma$ -point. We used  $6 \times 6 \times 1$  supercells for the systems with the

hexagonal primitive cells and  $4 \times 4 \times 1$  supercells for the tetragonal unit cell systems. In both cases, the Brillouin zone was sampled using the sole  $\Gamma$ -point.

## 3 Results

### 3.1 Phonon dispersions

The point symmetry group for dynamic configurations of nonmagnetic and Néel antiferromagnetic phases is  $D_{3d}$  (i.e., when  $M = \text{Mg, Mn, Zn, or Cd}$ ). The character table, Table 2, for the triangular unit cell at the  $\Gamma$ -point predicts 30 vibrational modes corresponding to irreducible representations as  $3A_{1g} + 2A_{2g} + 5E_g + A_{1u} + 4A_{2u} + 5E_u$ . Five  $E_g$  and three  $A_{1g}$  modes are Raman-active, four  $E_u$  and three  $A_{2u}$  are IR-active, one  $A_{2u}$  and one  $E_u$  are acoustic,  $A_{2g}$  and  $A_{1u}$  modes are optically inactive.

To analyze the vibrational properties of different modes, we start by showing phonon dispersion relations along the high-symmetry directions in the Brillouin zone and the phonon density of states (DOS) in Fig. 2. The contributions from each element are quantified by projecting the phonon eigenvector  $\phi$  to each of the atoms. For instance, the contribution from metal atoms is calculated as

$$|\phi_M|^2 = \sum_i |\phi_{i,x}|^2 + |\phi_{i,y}|^2 + |\phi_{i,z}|^2 \quad (1)$$

where  $\phi_{i,\alpha}$  denotes the eigenvector of atom  $i$  in the  $\alpha$ -direction, and the sum goes over all metal atoms. Contributions of phosphorus ( $|\phi_P|^2$ ) and chalcogen ( $|\phi_X|^2$ ) atoms are determined similarly. The contributions are normalized so that  $|\phi_{tot}|^2 = |\phi_M|^2 + |\phi_P|^2 + |\phi_X|^2 = 1$ . The atomic displacements for all Raman-active modes are presented in Appendix A in the case of  $\text{ZnPS}_3$ .

The dispersion curves show a few common features. First, since there are no imaginary frequency modes, all materials are dynamically stable. Second, as expected for 2D materials, there are two acoustic modes with linear  $q$ -dependences corresponding to the transversal and longitudinal modes within the plane,

Table 2: Character tables of irreducible representations and symmetry operation classes for  $D_{3d}$  and  $C_{2h}$  point symmetry groups.<sup>31</sup>

$D_{3d}$	$E$	$2C_3$	$3C_2$	$i$	$2S_6$	$3\sigma_h$	Linear, rotations	Quadratic
$A_{1g}$	1	1	1	1	1	1		$x^2 + y^2, z^2$
$A_{2g}$	1	1	-1	1	1	-1	$R_z$	
$E_g$	2	-1	0	2	-1	0	$(R_x, R_y)$	$(x^2 - y^2, xy)(xz, yz)$
$A_{1u}$	1	1	1	-1	-1	-1		
$A_{2u}$	1	1	-1	-1	-1	1	$z$	
$E_u$	2	-1	0	-2	1	0	$(x, y)$	

$C_{2h}$	$E$	$C_2$	$i$	$\sigma_h$	Linear, rotations	Quadratic
$A_g$	1	1	1	1	$R_z$	$x^2, y^2, z^2, xy$
$B_g$	1	-1	1	-1	$R_x, R_y$	$xy, yz$
$A_u$	1	1	-1	-1	$z$	
$B_u$	1	-1	-1	1	$x, y$	

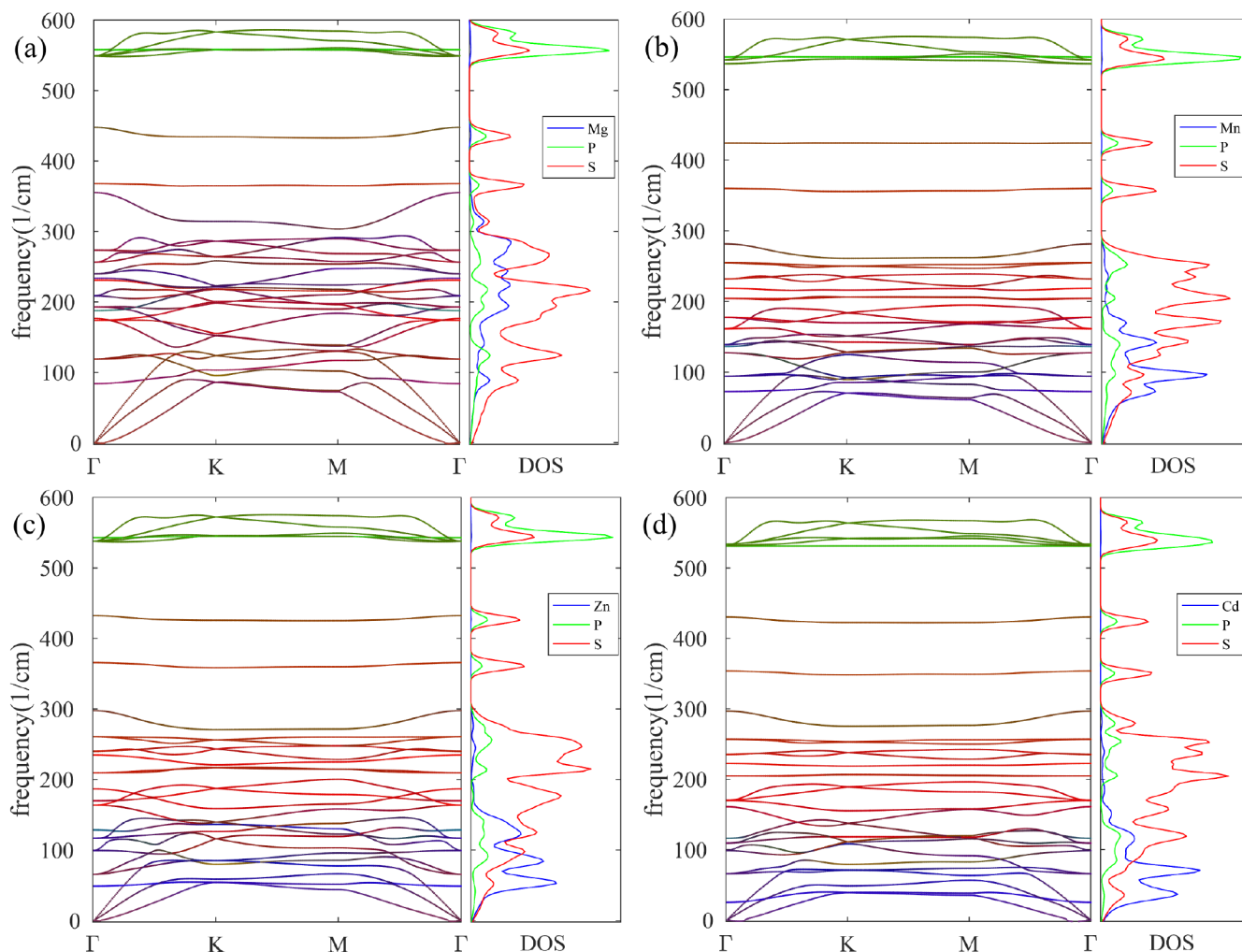


Figure 2: Phonon dispersion curves between high symmetry points,  $\Gamma$ ,  $K$ ,  $M$ , together with the corresponding partial phonon DOSs; (a)  $\text{MgPS}_3$ , (b)  $\text{MnPS}_3$ , (c)  $\text{ZnPS}_3$ , and (d)  $\text{CdPS}_3$ . Blue, green, and red denote projection to metal, phosphorus, and chalcogen atoms, respectively.



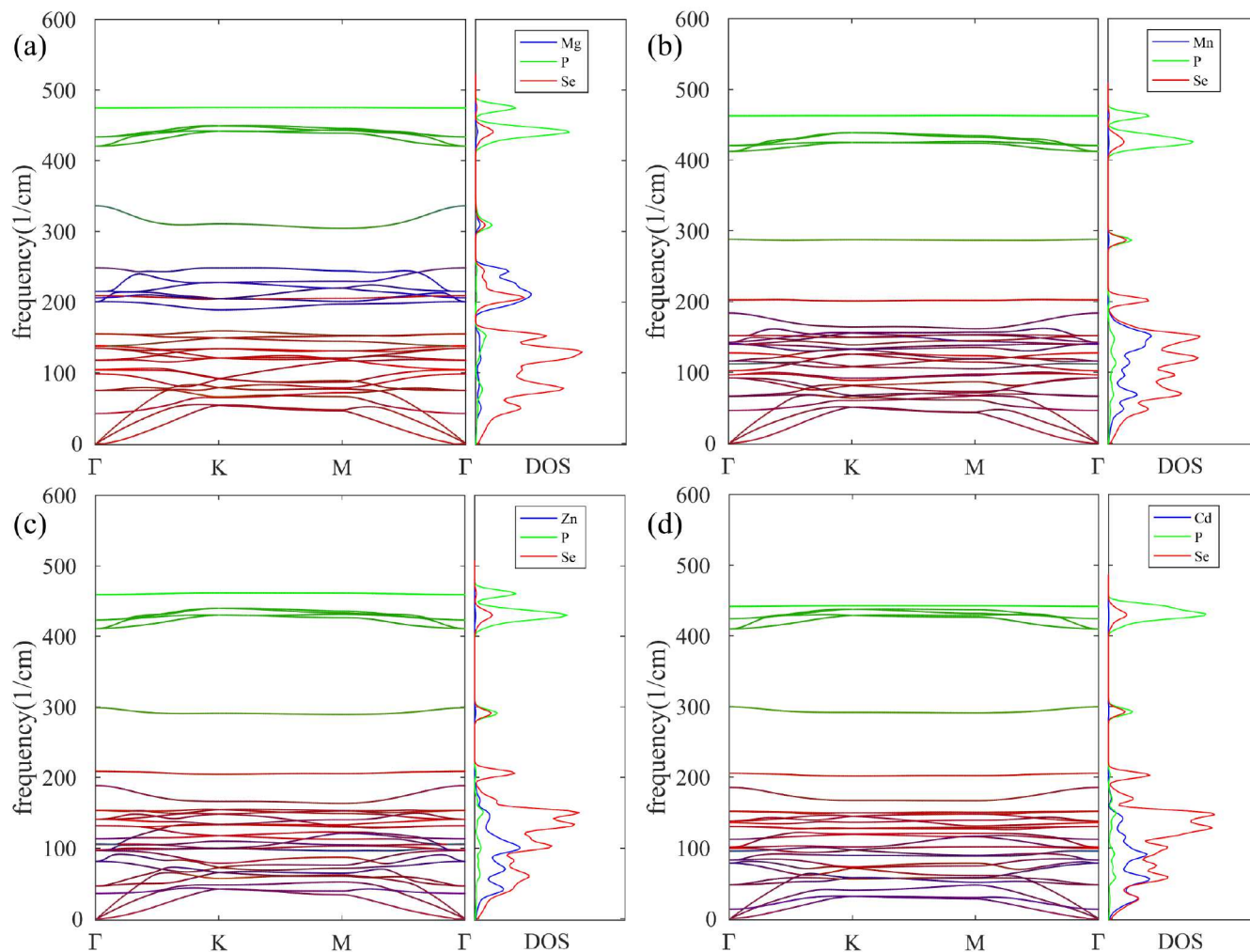


Figure 3: Phonon dispersion curves between high symmetry points,  $\Gamma$ ,  $K$ ,  $M$ , together with the corresponding partial phonon DOSs; (a)  $\text{MgPSe}_3$ , (b)  $\text{MnPSe}_3$ , (c)  $\text{ZnPSe}_3$ , and (d)  $\text{CdPSe}_3$ . Blue, green, and red denote projection to metal, phosphorus, and chalcogen atoms, respectively.

and one mode with a quadratic dependence describing the out-of-plane flexural response to the stress when one tries to bend the 2D plate. Third, all plots show similar orderings of the most significant atomic contributions as a function of the mode frequency. In  $\text{MPS}_3$  (except  $M = \text{Mg}$ ), the metal, chalcogen, and phosphorus contributions mostly play role at low, middle, and high frequencies. When comparing materials of different elements, the shift of the frequencies can be intuitively understood on the basis of different atomic masses. The only exception seems to be the case of  $\text{MgPSe}_3$ , where the metal atoms are markedly lighter than the chalcogen atoms. In more detail, there is (i) a manifold of states from 0 to  $300 \text{ cm}^{-1}$  in sulfides and from 0 to  $200 \text{ cm}^{-1}$  in selenides, (ii)

two flat bands at around  $370$  and  $430 \text{ cm}^{-1}$  in sulfides and around  $200$  and  $300 \text{ cm}^{-1}$  in selenides, and (iii) a set of bands between  $500$  and  $600 \text{ cm}^{-1}$  in sulfides and between  $400$  and  $500 \text{ cm}^{-1}$  in selenides. Frequencies of both the flat bands and the high frequency bands are largely independent of the metal atoms. The high frequency bands originate from the vibrations of the  $\text{P}_2$  dimer (cf. the displacements of modes  $A_{1g}^3$  and  $E_g^5$  in Fig. 6). The two flat bands arise from breathing modes of the  $\text{P}_2\text{S}_6$  cluster, where the chalcogen atoms in the top and bottom layer move either symmetrically ( $A_{1g}$ , lower frequency mode, cf. mode  $A_{1g}^3$  in Fig. 6) or antisymmetrically ( $A_{2u}$ , higher frequency mode).

Due to the zigzag AFM ordering in the case



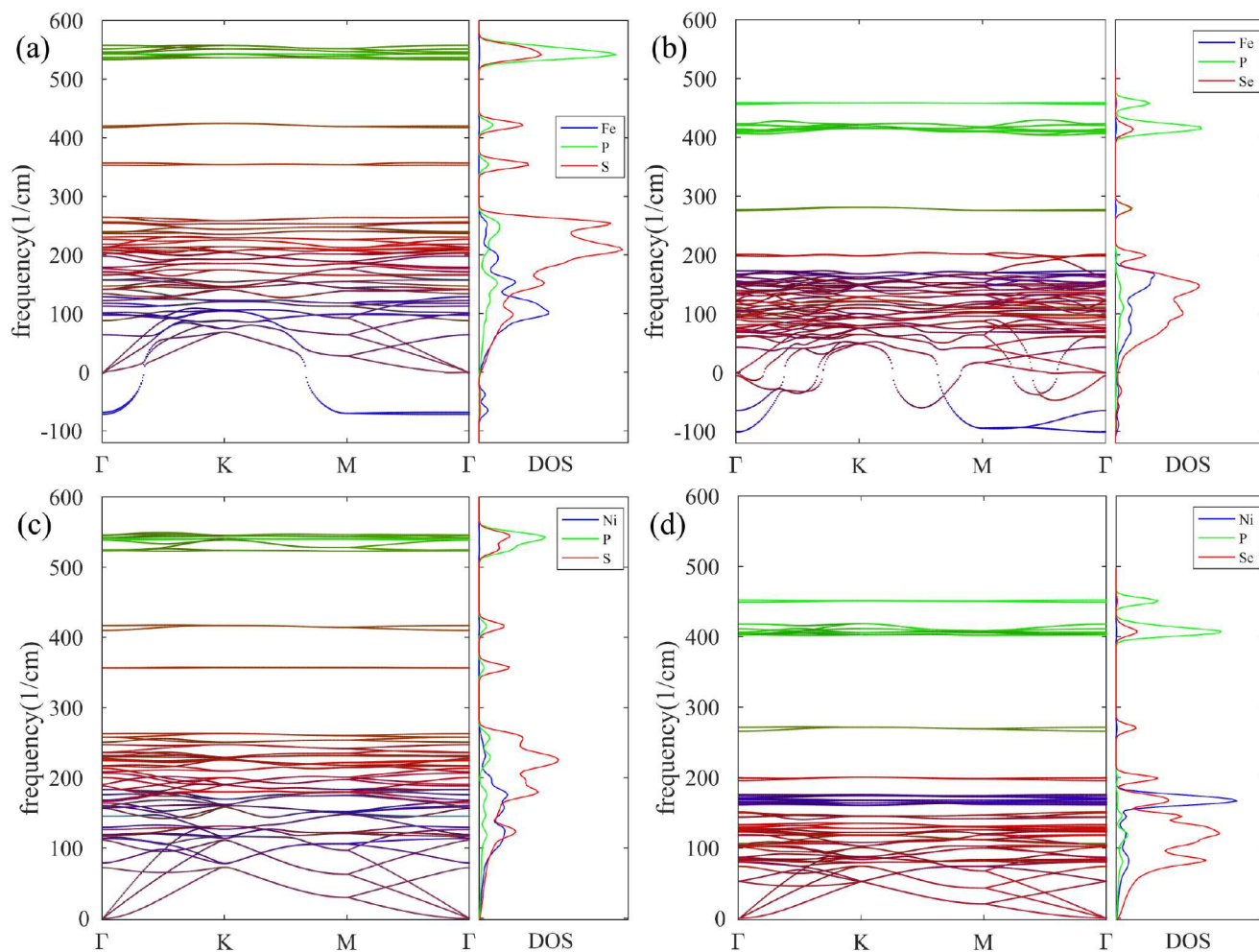


Figure 4: Phonon dispersion curves between high symmetry points,  $\Gamma[0,0,0] : K[0.5,0.5,0] : M[0,0.5,0]$ , together with the corresponding partial phonon DOSs; (a) FePS<sub>3</sub>, (b) FePSe<sub>3</sub>, (c) NiPS<sub>3</sub>, and (d) NiPSe<sub>3</sub>. Blue, green, and red denote projection to metal, phosphorus, and chalcogen atoms, respectively.

of FePX<sub>3</sub> and NiPX<sub>3</sub> the point group of the lattice is reduced to  $C_{2h}$  (cf. character table in Table 2) and due to the larger supercell the number of vibrational modes is 60. The irreducible representations at the  $\Gamma$ -point are  $16A_g + 14A_u + 12B_g + 18B_u$ , where the  $A_g$  and  $B_g$  modes are Raman active, one  $A_u$  and two  $B_u$  modes are acoustic and the remaining ones are IR-active. Nevertheless, the phonon dispersions plotted in Figure 4 show largely all the same features as discussed above. FePS<sub>3</sub> and FePSe<sub>3</sub> have few imaginary modes related to the breaking of the symmetry along the ferromagnetically coupled zigzag chain of Fe atoms, as mentioned in the Methods section. The phonon dispersions for the distorted structures are shown in the Appendix for reference.

### 3.2 Non-resonant Raman spectra

The Raman intensity  $I$  of a phonon mode is proportional to  $|\mathbf{e}_s^T \cdot \mathbf{R} \cdot \mathbf{e}_i|^2$ ,<sup>31</sup> where  $\mathbf{e}_s$  and  $\mathbf{e}_i$  are the electric polarization vectors of the scattered and incident light, respectively, and superscript  $T$  of  $\mathbf{e}_s$  denotes transpose. The Raman tensor  $\mathbf{R}$  is a second rank tensor calculated as the derivative of the polarizability with respect to the normal mode coordinates.<sup>32,33</sup> The  $D_{3d}$  point symmetry group dictates that the Raman tensors for the  $A_{1g}$  and  $E_g$  active modes can be expressed as:<sup>31</sup>

$$\mathbf{R}(A_{1g}) = \begin{bmatrix} a & \cdot & \cdot \\ \cdot & a & \cdot \\ \cdot & \cdot & b \end{bmatrix} \quad (2)$$

$$\mathbf{R}(E_g) = \begin{bmatrix} \cdot & c & \cdot \\ c & \cdot & d \\ \cdot & e & \cdot \end{bmatrix}, \begin{bmatrix} c & \cdot & -d \\ \cdot & -c & \cdot \\ -e & \cdot & \cdot \end{bmatrix} \quad (3)$$

where  $a$ – $e$  are the major terms. The other terms denoted by " $\cdot$ " are expected to be zero on the basis of symmetry, while a minor contribution may be obtained in calculations due to numerical inaccuracies.

As commonly adopted in Raman spectroscopy of 2D materials,<sup>17,34</sup> we consider the back-scattering configuration, in which the incident light moves along the  $z$ -axis and the polarization vectors within the  $xy$  plane are  $\mathbf{e}_i^T = (\cos\theta, \sin\theta, 0)$  and  $\mathbf{e}_s^T = (\cos\phi, \sin\phi, 0)$ , where  $\theta$  and  $\phi$ , respectively, are the angles of the incident and scattered electric polarization vectors with  $x$ -axis in detectors. Thus,

$$I(A_{1g}) = a^2 \cos^2(\phi - \theta) \quad (4)$$

$$I(E_g) = c^2 [\sin^2(\theta + \phi) + \cos^2(\theta + \phi)] = c^2.$$

Based on the above relations,  $A_{1g}$  modes depend on the polarization change between the incident and scattered light, but for  $E_g$  modes the angle dependence vanishes. In order to have the maximum possible amount of intensity for each mode, we fix the polarization vectors to the parallel configuration  $\theta = \phi$ , whereby  $I(A_{1g}) = a^2$  and  $I(E_g) = c^2$ .

For the  $C_{2h}$  point group, the tensors are:

$$\mathbf{R}(A_g) = \begin{bmatrix} a & \cdot & d \\ \cdot & b & \cdot \\ d & \cdot & c \end{bmatrix} \quad (5)$$

$$\mathbf{R}(B_g) = \begin{bmatrix} \cdot & e & \cdot \\ e & \cdot & f \\ \cdot & f & \cdot \end{bmatrix} \quad (6)$$

and the intensities

$$\begin{aligned} I(A_g) &= |a \cos \theta \cos \phi + b \sin \theta \sin \phi|^2 \\ I(B_g) &= |e \sin \theta \cos \phi + f \cos \theta \sin \phi|^2. \end{aligned} \quad (7)$$

We note that even when we assume the paral-

lel configuration  $\theta = \phi$ , the dependence on the polarization angle is retained when  $a \neq b$ .

The calculated Raman spectra are shown in Fig. 5 (with the artificial broadening of  $4 \text{ cm}^{-1}$  to mimic the experimental spectra), and the absolute values of  $I$  are listed in Table 3. Overall, a drastic sensitivity to the chalcogen anion is evident, whereas the spectra appear fairly insensitive to the metal cation, except for the two lowest  $E_g$  modes, which have the strongest contributions from the metal atoms.

The spectra of the  $D_{3d}$  systems are discussed next with the help of the schematic representations of the displacements shown in Fig. 6 in the case of  $\text{ZnPS}_3$ . We start from the two low frequency  $E_g$  Raman modes,  $E_g^1$  corresponds to rotation of the  $\text{P}_2\text{X}_6$  cluster and  $E_g^2$  to an in-plane optical mode involving metal atoms. They are sensitive to the metal atom, but the Raman activities are small. Next, there is a group of two  $E_g$  modes and one  $A_{1g}$  mode, with medium Raman activities depending on the material.  $E_g^3$  and  $E_g^4$  modes correspond to the stretching of the  $\text{P}_2\text{X}_6$  cluster and the  $A_{1g}^1$  mode to a breathing mode involving chalcogen atoms displaced out-of-plane. The most intense Raman peak is  $A_{1g}^2$ , which can be considered as a breathing mode of the  $\text{P}_2\text{X}_6$  cluster. Finally, there are high-frequency modes including the  $\text{P}_2$  stretching mode  $A_{1g}^3$  with a medium activity and a low activity  $E_g^5$  mode corresponding to the rotation of the  $\text{P}_2$  dimer.

Experimental data on monolayer TMPTs is still very scarce, but a comparison of our results with bulk spectra reveals an overall agreement. First of all, due to the underbinding by the PBE functional, as also seen in the overestimation of the lattice constants, the calculated frequencies are generally lower than the experimental values. In an early study,<sup>35</sup> Bernasconi et al. presented room temperature Raman spectra for  $\text{MnPS}_3$ ,  $\text{NiPS}_3$ ,  $\text{ZnPS}_3$ ,  $\text{FePS}_3$ , and  $\text{FePSe}_3$ . All the sulfides showed strong peaks at around  $280$  and  $390 \text{ cm}^{-1}$ , with the former accompanied by one or two weaker peaks at some tens of  $\text{cm}^{-1}$  lower wavenumbers. Based on our calculations, the pronounced peaks are assigned to  $E_g^4$  and  $A_{1g}^2$  modes, respectively, and the weaker features to  $E_g^3$  and  $A_{1g}^1$  modes. Peaks with smaller

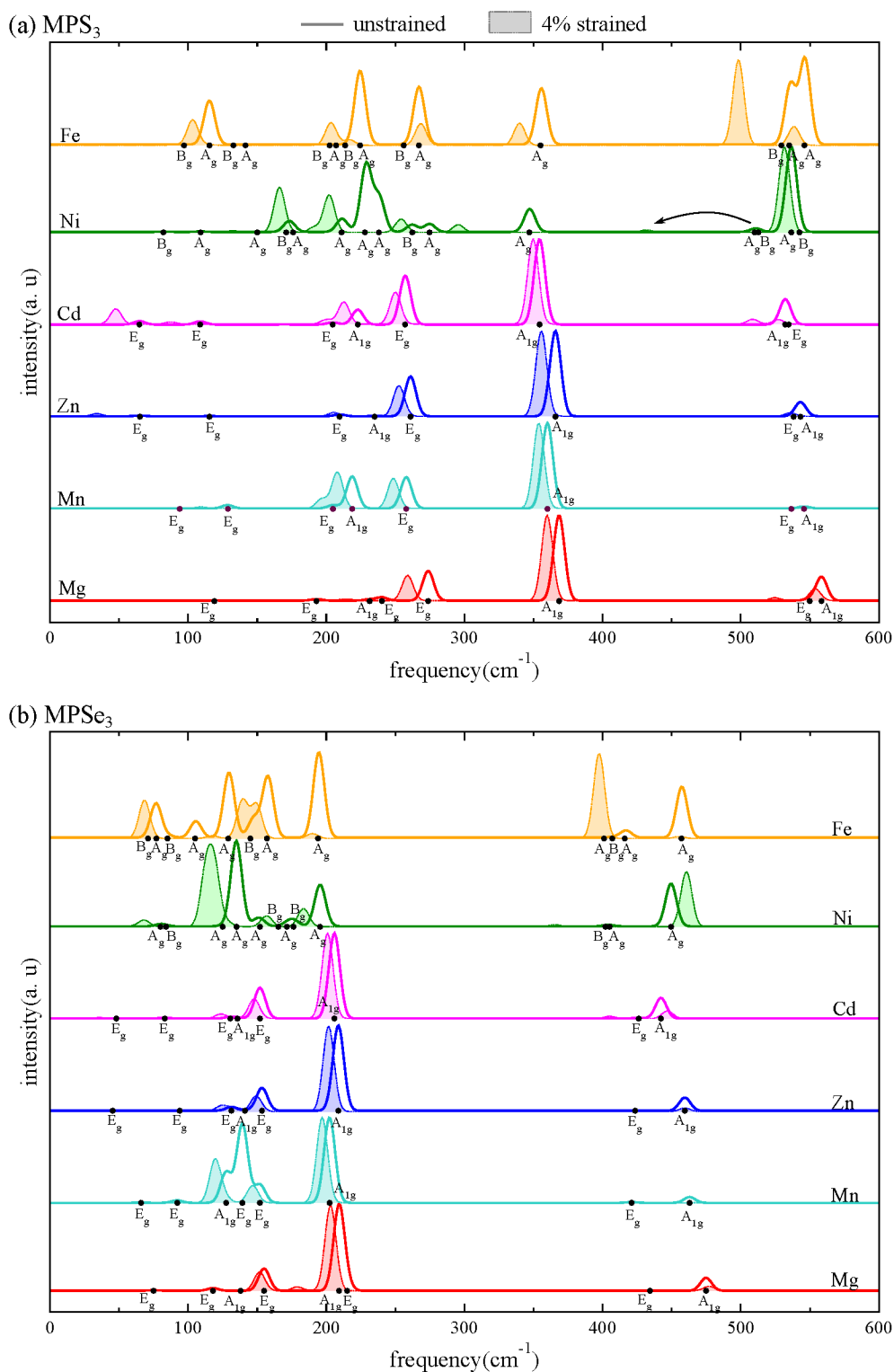


Figure 5: Normalized Raman spectra in the parallel configuration for (a) sulfides and (b) selenides, both in the cases of unstrained (solid line) and 4 % strained (shaded regions) lattices. The dots depict frequencies that are expected to have raman-active modes and the corresponding irreducible representations are also denoted. The black arrow for  $\text{NiPS}_3$  indicates the origin of the weak peak appearing at  $430 \text{ cm}^{-1}$ .

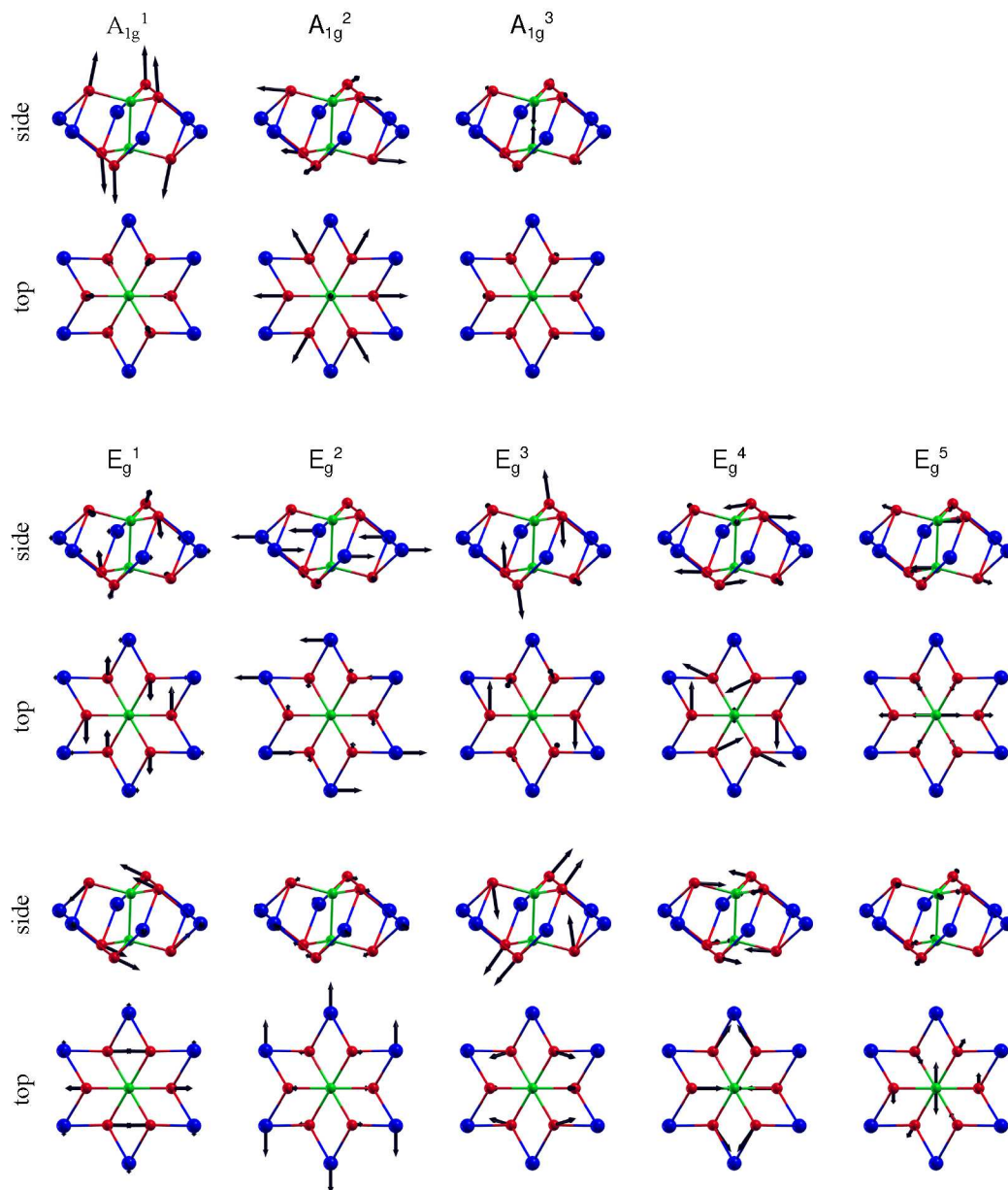


Figure 6: Schematic representations of atomic displacements of eight Raman-active modes as top and side views. The superscripts denote the indexing of the modes within the same symmetry. Two figures are shown for each of the doubly degenerate  $E_g$  modes. Blue, green, and red balls denote metal, phosphorus, and chalcogen atoms, respectively. Arrows are proportional to the displacements and come from the real part of the eigenvectors at the  $\Gamma$ -point. The sizes and orientations of the arrows correspond to the magnitudes and directions of the displacement vectors.

intensities were found below  $200\text{ cm}^{-1}$ , likely corresponding to  $E_g^1$  and  $E_g^2$  modes, but varying from system to system, and weak features around  $580\text{ cm}^{-1}$  corresponding to  $E_g^4$  and  $A_{1g}^3$  modes.

The overall good agreement with the experimental results for bulk systems is not surprising, as the vibrational modes are largely confined to the layers and there is little interaction

between the layers. This has also been verified experimentally in few cases. For  $\text{NiPS}_3$ , Kuo et al. obtained the spectra for bulk and 2–7 layers,<sup>36</sup> showing little variation with respect to the number of layers. Similar conclusions were reached for  $\text{FePX}_3$ .<sup>6,37</sup> While less data is available for selenides, similar conclusions are expected to hold.

The calculated Raman spectra for the  $C_{2h}$



compounds,  $\text{FePX}_3$  and  $\text{NiPX}_3$ , needs to be discussed separately. Overall the results for symmetric  $\text{FePX}_3$  are still largely in line with those for the  $D_{3d}$  compounds. The assignments become more complicated due to a larger number of Raman active modes, but the most intense features are expected to arise from similar phonon modes. Moreover, these primary modes are found in both the symmetric and distorted phases, as presented in the Appendix.

The  $\text{NiPX}_3$  spectra appear little different from the rest, even though the structures were found to be symmetric without imaginary frequency modes. The experimental results of Bernasconi et al. showed the same intense features as the other TMPTs, but also several additional intense peaks below  $200\text{ cm}^{-1}$  and between  $400$  and  $600\text{ cm}^{-1}$ . In the calculated spectra, the high frequency modes are in accordance with the other materials. In addition, we see several Raman active modes between  $150$  and  $300\text{ cm}^{-1}$ , but it is difficult to assign these to the experimentally observed modes at this frequency range.

Raman spectroscopy is often used to probe the strain of the material, and thus we will next consider how Raman spectra change in response to the biaxial tensile strain. The shift of the Raman-active mode frequencies as a function of the applied strain are shown in Fig. 7 in the case of  $\text{CdPS}_3$  and  $\text{CdPSe}_3$ . Within the studied range of strain values (1–4 %), the frequencies exhibit linear dependence on strain. The gradients of the frequencies  $d\omega/d\epsilon$  are also listed in Table 3. In addition, the shaded regions in Fig. 5 indicate Raman spectra of the materials under a 4 % strain and give a quick visual indication of the changes. As expected, stretching weakens the bonds and consequently the frequencies shift to lower wavenumbers. The only exception is the  $A_{1g}^3$  mode in the case of selenides, which involves only out-of-plane movement of the P atoms (cf. Fig. 6). Thus, the positive gradient could be rationalized such that the tensile strain leads to reduction of the layer thickness  $d$ , which consequently allows for strengthening of the P-P bond. The most prominent  $E_g^4$  and  $A_{1g}^2$  modes largely retain their intensities with frequency shifts of  $-1$  to  $-4\text{ cm}^{-1}$  per 1 % of strain

and thus should be applicable for analysing the strain of the sample. The magnitudes of these shifts are comparable to those found in other 2D materials. For instance, monolayer  $\text{MoS}_2$  upon application of biaxial strain, the  $E_{2g}^1$  mode shifted by  $-5.2\text{ cm}^{-1}/\%$  and the  $A_{1g}$  mode by  $-1.7\text{ cm}^{-1}/\%$ .<sup>38</sup> Graphene, on the other hand, shows a much larger shift in the G-mode, i.e.,  $-63\text{ cm}^{-1}/\%$ .<sup>39</sup>

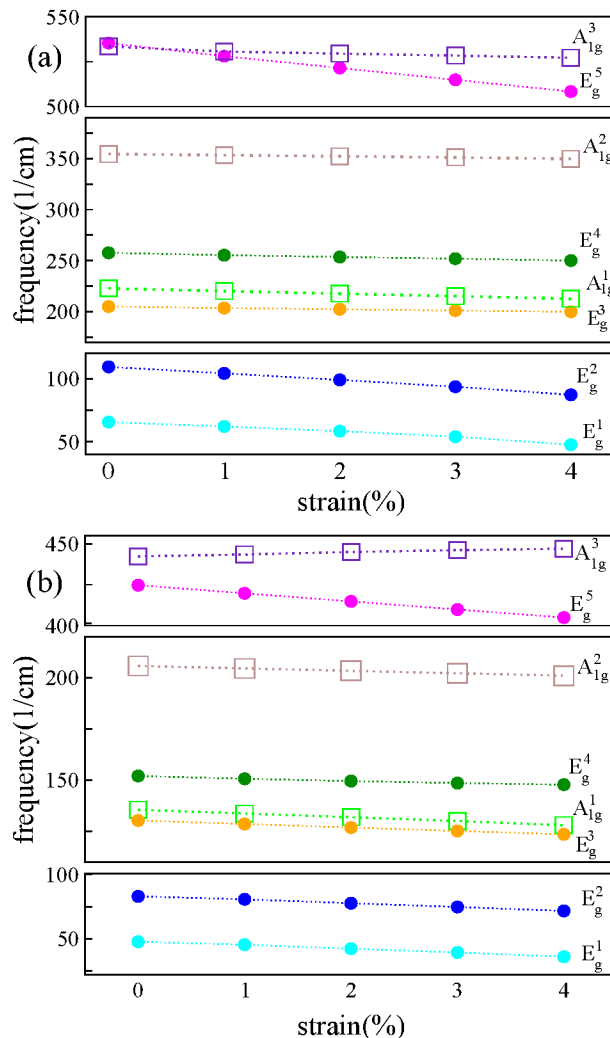


Figure 7: Effect biaxial strain (0–4 %) on the frequencies of Raman-active modes; (a)  $\text{CdPS}_3$  and (b)  $\text{CdPSe}_3$ . The slope of the linear fitting for all the materials and modes is reported in Table 1.

### 3.3 Elastic constants

To finalize our study on the mechanical properties of TMPT materials, we calculated the

**Table 3: Frequencies  $\omega$ , Raman intensities  $I$ , and the frequency gradients  $d\omega/d\epsilon$  for the Raman-active modes. The frequency shifts are in the units of  $\text{cm}^{-1}/\%$ .**

		MgPS <sub>3</sub>	MgPSe <sub>3</sub>	MnPS <sub>3</sub>	MnPSe <sub>3</sub>	ZnPS <sub>3</sub>	ZnPSe <sub>3</sub>	CdPS <sub>3</sub>	CdPSe <sub>3</sub>
A <sub>1g</sub> <sup>1</sup>	$\omega$	230.9	137.9	218.7	127.4	234.9	141.1	222.7	135.6
	$I$	0.53	0.007	0.61	0.6	0.036	0.002	0.39	0.069
	$d\omega/d\epsilon$	-11.77	-0.62	-2.61	-4.22	-3.25	-1.52	-2.55	-1.86
A <sub>1g</sub> <sup>2</sup>	$\omega$	368	209	360	202.3	365.7	208.6	354.3	205.8
	$I$	1.0	1.0	1.0	1.0	1.0	1.0	1.0	1.0
	$d\omega/d\epsilon$	-2.08	-1.55	-1.66	-1.33	-2.54	-1.72	-1.15	-1.18
A <sub>1g</sub> <sup>3</sup>	$\omega$	557.9	474.6	545.8	462.9	543.1	459.4	532.1	442.1
	$I$	0.104	0.39	0.15	0.26	0.41	0.39	0.55	0.5
	$d\omega/d\epsilon$	-1.12	0.53	-0.49	1.66	-1.82	-0.02	-1.47	1.2
E <sub>g</sub> <sup>1</sup>	$\omega$	118.8	74.9	93.9	65.8	65.1	45.4	64.7	47.9
	$I$	0.029	0.056	0.033	0.045	0.077	0.0003	0.16	0.034
	$d\omega/d\epsilon$	-5.21	-2.89	-2.75	-1.63	-7.52	-2.18	-4.39	-2.94
E <sub>g</sub> <sup>2</sup>	$\omega$	192.9	117.8	128.7	92.07	115.3	93.8	108.6	83.1
	$I$	0.88	0.13	0.15	0.71	0.041	0.015	0.16	0.071
	$d\omega/d\epsilon$	-3.59	-0.05	-4.40	-0.11	-7.52	-4.03	-5.48	-2.86
E <sub>g</sub> <sup>3</sup>	$\omega$	239.9	155	204.8	139.2	209.5	131.2	204.6	130.5
	$I$	0.15	0.15	0.016	0.14	0.1	0.17	0.055	0.1
	$d\omega/d\epsilon$	-5.31	-0.9	-1.86	-3.26	-1.04	-1.93	-1.24	-1.68
E <sub>g</sub> <sup>4</sup>	$\omega$	273.5	214.9	254.8	151.8	260.9	153.4	257.1	151.9
	$I$	0.42	0.18	0.48	0.37	0.54	0.41	0.61	0.48
	$d\omega/d\epsilon$	-3.84	-9.02	-1.62	-1.29	-2.2	-1.09	-1.86	-1.06
E <sub>g</sub> <sup>5</sup>	$\omega$	549.5	433.7	536.5	420.9	538.2	423.5	534.6	426.1
	$I$	0.114	0.013	0.022	0.076	0.01	0.03	0.036	0.048
	$d\omega/d\epsilon$	-6.27	-4.57	-6.69	-4.99	-8.12	-5.68	-6.71	-4.92

elastic tensor with three non-trivial independent coefficients  $C_{11}$ ,  $C_{12}$ , and  $C_{44}$ . In addition, we determined  $C_{shear} = (C_{11} - C_{12})/2$ ,  $Y_s = (C_{11}^2 + C_{12}^2)/C_{11}$ ,  $\nu = C_{12}/C_{11}$ . The results are listed in Table 4. The selenides show consistently slightly smaller elastic constants than the respective sulfides, but overall all TMPTs exhibit roughly similar values. More interestingly, a comparison with other 2D materials reveals that these materials are soft exhibiting, e.g., Young's modulus of roughly half of that for MoS<sub>2</sub> and one fourth of that for graphene. Only MgPX<sub>3</sub> shows a  $\nu$  value comparable to MoS<sub>2</sub>, whereas all the other TMPTs show high Poisson ratios of 0.3–0.4.

## 4 Conclusions

We have carried out extensive first-principles calculations of the mechanical and vibrational properties of monolayer TMPTs MPX<sub>3</sub> (M = Mg, Mn, Fe, Ni, Zn, or Cd; X = S or Se). We analyzed their dynamical stabilities and atomic characters of the vibrational modes. The Raman spectra of the unstrained and strained layers were calculated, and the nature of the Raman active modes was discussed in detail. The softening rate of the modes upon strain can be used to identify the degree of strain in the samples measured experimentally. Finally, we assessed the elastic properties, showing that these materials are softer than many other layered materials, which should be taken into account to optimize the exfoliation process.



**Table 4: Calculated elastic constants and comparison to few other common 2D materials. Elastic constant  $C_{11}$ ,  $C_{12}$ , and Young’s modulus  $Y_s$  are in the units of N/m. The Poisson ratio  $\nu$  is unitless.**

	$C_{11}$	$C_{12}$	$C_{shear}$	$Y_s$	$\nu$
MgPS <sub>3</sub>	65.4	17.4	24.0	70.0	0.266
MgPSe <sub>3</sub>	55.7	15.4	20.1	59.9	0.277
MnPS <sub>3</sub>	61.7	20.2	20.8	68.3	0.327
MnPSe <sub>3</sub>	53.2	18.6	17.3	59.7	0.350
FePS <sub>3</sub>	72.7	22.1	25.0	79.4	0.304
FePSe <sub>3</sub>	61.9	19.4	22.0	67.9	0.312
NiPS <sub>3</sub>	87.0	23.1	31.9	93.1	0.265
NiPSe <sub>3</sub>	73.3	20.1	26.7	78.8	0.275
ZnPS <sub>3</sub>	67.5	27.1	20.2	78.4	0.401
ZnPSe <sub>3</sub>	58.3	22.9	17.7	67.4	0.393
CdPS <sub>3</sub>	53.6	20.6	16.5	61.6	0.385
CdPSe <sub>3</sub>	47.0	17.9	14.5	53.8	0.381
MoS <sub>2</sub>	137.9	36.0	50.9	147.3	0.262
graphene	352.6	59.6	146.5	362.67	0.17

## Acknowledgments

We thank the Academy of Finland for the support under Project No. 286279, and through its Centres of Excellence Programme (2012-2017) under Project No. 251748. We also thank CSC-IT Center for Science Ltd. and Aalto Science-IT project for generous grants of computer time.

## A Appendix: Comparison between the symmetric and distorted structures of FePX<sub>3</sub>

The phonon dispersions from the symmetric and distorted structures are shown in Fig. 8 for FePS<sub>3</sub> and FePSe<sub>3</sub>. The symmetric structure shows few imaginary modes, which correspond to breaking of the symmetry in the Fe-Fe bonds along the zigzag chain of parallel magnetic moments (cf. the rectangular unit cell in Fig. 1). The distorted structures, obtained by displacing the atoms according to these imaginary modes and relaxing the struc-

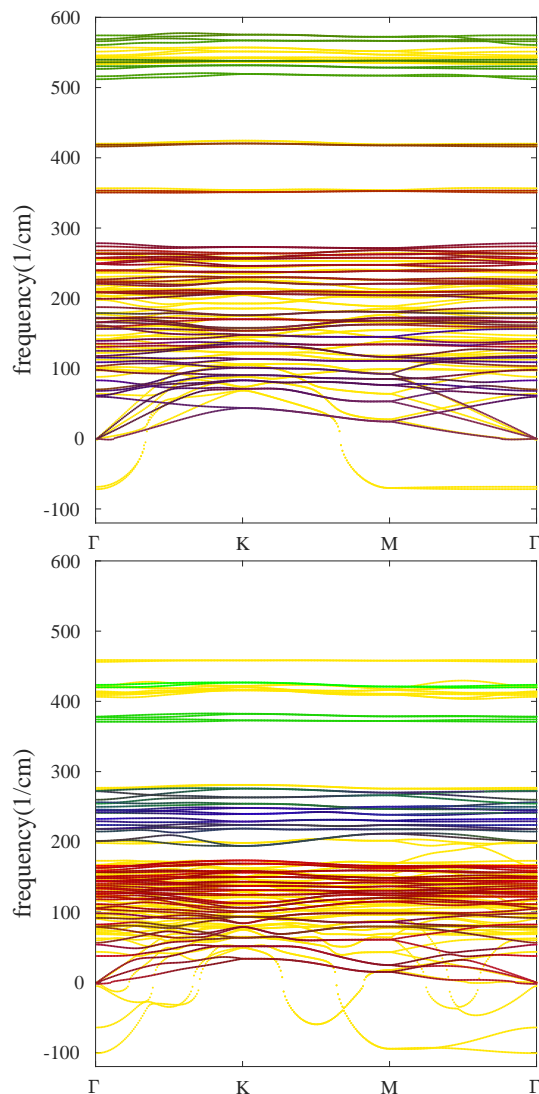


Figure 8: Comparison of the phonon dispersion curves for FePS<sub>3</sub> (top) and FePSe<sub>3</sub> (bottom), in the symmetric and distorted structures. The symmetric ones are the same as shown in Fig. 4(a,b) and colored by yellow. The distorted structure is colored according to the projection to the atoms as previously.

ture again, are free of imaginary modes. The high-frequency modes, originating either from the P<sub>2</sub> or P<sub>2</sub>X<sub>6</sub> displacements, are only weakly affected by the distortion involving the Fe-Fe bonds.

Comparison of the calculated (PBE) Raman spectra of the symmetric and distorted structures for the FePS<sub>3</sub> monolayer to the experimental ones<sup>6</sup> is presented in Fig. 9. The highest peak is not recorded in the experimental spectrum. In addition, the results from PBE+U

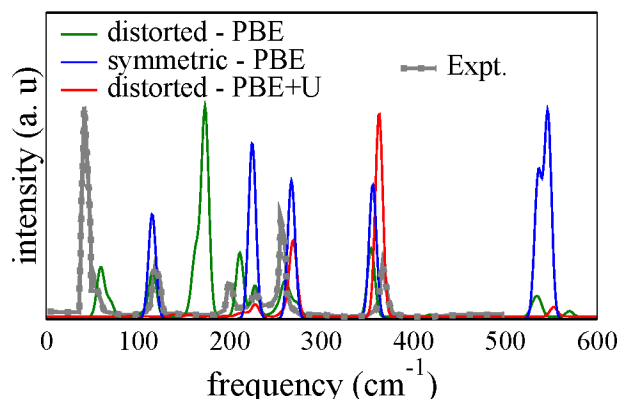


Figure 9: Comparison of the experimental Raman spectra of FePS<sub>3</sub> (data from Ref.<sup>6</sup>) with the calculated ones from distorted and symmetric structures and also calculated using the PBE+U method.

calculations are shown, where a  $U$  parameter of 3.5 eV is used for the Fe  $d$ -orbitals. The parameter was chosen to yield the same energy difference between the FM and AFM configurations as in HSE calculations. Such a choice also almost completely removes the distortion. The main peaks at around 250 and 350  $\text{cm}^{-1}$  are found in all calculated spectra. The distorted structure gives perhaps a better overall agreement with the experimental spectra but also yields an intense extra feature at around 170  $\text{cm}^{-1}$ . The symmetric structure, on the other hand, fails to reproduce the peak at around 50  $\text{cm}^{-1}$  and shows only two peaks between 200 and 300  $\text{cm}^{-1}$  instead of three. The PBE+U approach seems to overall perform the worst. All the low frequency modes below 200  $\text{cm}^{-1}$  are either missing or show very small intensity. On the other hand, the third peak at around 200  $\text{cm}^{-1}$  is present, although with weak intensity.

## References

- (1) Li, X.; Cao, T.; Niu, Q.; Shi, J.; Feng, J. Coupling the Valley Degree of Freedom to Antiferromagnetic Order. *Proceedings of the National Academy of Sciences* **2013**, *110*, 3738–3742.
- (2) Ressouche, E.; Loire, M.; Simonet, V.; Ballou, R.; Stunault, A.; Wildes, A. Mag-

netoelectric MnPS<sub>3</sub> as a Candidate for Ferrotoroidicity. *Phys. Rev. B* **2010**, *82*, 100408.

- (3) Wildes, A. R.; Rule, K. C.; Bewley, R. I.; Enderle, M.; Hicks, T. J. The Magnon Dynamics and Spin Exchange Parameters of FePS<sub>3</sub>. *Journal of Physics: Condensed Matter* **2012**, *24*, 416004.
- (4) Liu, J.; Li, X.-B.; Wang, D.; Lau, W.-M.; Peng, P.; Liu, L.-M. Diverse and Tunable Electronic Structures of Single-Layer Metal Phosphorus Trichalcogenides for Photocatalytic Water Splitting. *The Journal of Chemical Physics* **2014**, *140*, 054707.
- (5) Wildes, A. R.; Rønnow, H. M.; Roessli, B.; Harris, M. J.; Godfrey, K. W. Static and Dynamic Critical Properties of the Quasi-Two-Dimensional Antiferromagnet MnPS<sub>3</sub>. *Phys. Rev. B* **2006**, *74*, 094422.
- (6) Du, K.-z.; Wang, X.-z.; Liu, Y.; Hu, P.; Utama, M. I. B.; Gan, C. K.; Xiong, Q.; Kloc, C. Weak van der Waals Stacking, Wide-Range Band Gap, and Raman Study on Ultrathin Layers of Metal Phosphorus Trichalcogenides. *ACS Nano* **2016**, *10*, 1738–1743.
- (7) Kuo Cheng-Tai.; Neumann Michael.; Balamurugan Karuppanan.; Park Hyun Ju.; Kang Soonmin.; Shiu Hung Wei.; Kang Jin Hyoun.; Hong Byung Hee.; Han Moon-sup.; Noh Tae Won, et al. Exfoliation and Raman Spectroscopic Fingerprint of Few-Layer NiPS<sub>3</sub> van der Waals Crystals. *Scientific Reports* **2016**, *6*, 20904.
- (8) Py, M. A.; Haering, R. R. Structural Destabilization Induced by Lithium Intercalation in MoS<sub>2</sub> and Related Compounds. *Canadian Journal of Physics* **1983**, *61*, 76–84.
- (9) Chhowalla, M.; Shin, H. S.; Eda, G.; Li, L.-J.; Loh, K. P.; Zhang, H. The Chemistry of Two-Dimensional Layered Transition Metal Dichalcogenide Nanosheets. *Nature Chemistry* **2013**, *5*, 263–275.

- (10) Joy, P. A.; Vasudevan, S. Magnetism in the Layered Transition-Metal Thiophosphates MPS<sub>3</sub> (M=Mn, Fe, And Ni). *Phys. Rev. B* **1992**, *46*, 5425–5433.
- (11) Ouvrard, G.; Brec, R.; Rouxel, J. Structural Determination of Some MPS<sub>3</sub> Layered Phases (M = Mn, Fe, Co, Ni And Cd). *Materials Research Bulletin* **1985**, *20*, 1181–1189.
- (12) Zhang, X.; Zhao, X.; Wu, D.; Jing, Y.; Zhou, Z. MnPSe<sub>3</sub> Monolayer: A Promising 2D Visible-Light Photohydrolytic Catalyst with High Carrier Mobility. *Advanced Science* **2016**, *3*, 1600062.
- (13) Sivadas, N.; Okamoto, S.; Xiao, D. Gate-Controllable Magneto-Optic Kerr Effect in Layered Collinear Antiferromagnets. *Phys. Rev. Lett.* **2016**, *117*, 267203.
- (14) Li, X.; Wu, X.; Yang, J. Half-Metallicity in MnPSe<sub>3</sub> Exfoliated Nanosheet with Carrier Doping. *Journal of the American Chemical Society* **2014**, *136*, 11065–11069.
- (15) Gusmão, R.; Sofer, Z.; Sedmidubský, D.; Huber, Š.; Pumera, M. The Role of the Metal Element in Layered Metal Phosphorus Triselenides upon Their Electrochemical Sensing and Energy Applications. *ACS Catalysis* **2017**, *7*, 8159–8170.
- (16) Lee, J.-U.; Lee, S.; Ryoo, J. H.; Kang, S.; Kim, T. Y.; Kim, P.; Park, C.-H.; Park, J.-G.; Cheong, H. Ising-Type Magnetic Ordering in Atomically Thin FePS<sub>3</sub>. *Nano Letters* **2016**, *16*, 7433–7438.
- (17) Zhang, X.; Qiao, X.-F.; Shi, W.; Wu, J.-B.; Jiang, D.-S.; Tan, P.-H. Phonon and Raman Scattering of Two-Dimensional Transition Metal Dichalcogenides from Monolayer, Multilayer to Bulk Material. *Chem. Soc. Rev.* **2015**, *44*, 2757–2785.
- (18) Parkin, W. M.; Balan, A.; Liang, L.; Das, P. M.; Lamparski, M.; Naylor, C. H.; Rodríguez-Manzo, J. A.; Johnson, A. T. C.; Meunier, V.; Drndić, M. Raman Shifts in Electron-Irradiated Monolayer MoS<sub>2</sub>. *ACS Nano* **2016**, *10*, 4134–4142.
- (19) Eckmann, A.; Felten, A.; Mishchenko, A.; Britnell, L.; Krupke, R.; Novoselov, K. S.; Casiraghi, C. Probing the Nature of Defects in Graphene by Raman Spectroscopy. *Nano letters* **2012**, *12*, 3925–30.
- (20) Scheuschner, N.; Gillen, R.; Staiger, M.; Maultzsch, J. Interlayer Resonant Raman Modes in Few-Layer MoS<sub>2</sub>. *Phys. Rev. B* **2015**, *91*, 235409.
- (21) Sheremetyeva, N.; Cherniak, D. J.; Watson, E. B.; Meunier, V. Effect of pressure on the Raman-active modes of zircon (ZrSiO<sub>4</sub>): a first-principles study. *Physics and Chemistry of Minerals* **2017**,
- (22) F. Boucher, M. E.; Brec, R. Second Order Jahn-Teller Effect in CdPS<sub>3</sub> and ZnPS<sub>3</sub> Demonstrated by a Non-harmonic Behaviour of Cd<sup>2+</sup> and Zn<sup>2+</sup> d<sub>10</sub> Ions. *Journal of Alloys and Compounds* **1994**, *215*, 63–70.
- (23) Jörgens, S.; Mewis, A. Die Kristallstrukturen Von Hexachalcogeno-Hypodiphosphaten Des Magnesiums Und Zinks. *Zeitschrift für anorganische und allgemeine Chemie* **2004**, *630*, 51–57.
- (24) Zeng, R.; Wang, S. Q.; Du, G. D.; Wang, J. L.; Debnath, J. C.; Shamba, P.; Fang, Z. Y.; Dou, S. X. Abnormal Magnetic Behaviors and Large Magnetocaloric Effect in MnPS<sub>3</sub> Nanoparticles. *Journal of Applied Physics* **2012**, *111*, 07E144.
- (25) Kresse, G.; Hafner, J. Ab-Initio Molecular Dynamics for Liquid Metals. *Phys. Rev. B* **1993**, *47*, 558–561.
- (26) Rule, K. C.; McIntyre, G. J.; Kennedy, S. J.; Hicks, T. J. Single-Crystal and Powder Neutron Diffraction Experiments on FePS<sub>3</sub>: Search for the Magnetic Structure. *Phys. Rev. B* **2007**, *76*, 134402.

- 1  
2  
3  
4  
5  
6  
7  
8  
9  
10  
11  
12  
13  
14  
15  
16  
17  
18  
19  
20  
21  
22  
23  
24  
25  
26  
27  
28  
29  
30  
31  
32  
33  
34  
35  
36  
37  
38  
39  
40  
41  
42  
43  
44  
45  
46  
47  
48  
49  
50  
51  
52  
53  
54  
55  
56  
57  
58  
59  
60
- (27) Perdew, J. P.; Burke, K.; Ernzerhof, M. Generalized Gradient Approximation Made Simple. *Phys. Rev. Lett.* **1996**, *77*, 3865–3868.
- (28) Chittari, B. L.; Park, Y.; Lee, D.; Han, M.; MacDonald, A. H.; Hwang, E.; Jung, J. Electronic and Magnetic Properties of Single-Layer MPX<sub>3</sub> Metal Phosphorous Trichalcogenides. *Phys. Rev. B* **2016**, *94*, 184428.
- (29) Baroni, S.; de Gironcoli, S.; Dal Corso, A.; Giannozzi, P. Phonons and Related Crystal Properties from Density-Functional Perturbation Theory. *Rev. Mod. Phys.* **2001**, *73*, 515–562.
- (30) Togo, A.; Tanaka, I. First-Principles Phonon Calculations in Materials Science. *Scr. Mater.* **2015**, *108*, 1–5.
- (31) Cardona, M. *Light Scattering in Solids-I*; Berlin: Springer, 1983; Chapter 2.
- (32) Fonari, A.; Stauffer, S. *Vasp\_raman.py*; <https://github.com/raman-sc/VASP/>, 2013.
- (33) Porezag, D.; Pederson, M. R. Infrared Intensities and Raman-Scattering Activities within Density-Functional Theory. *Phys. Rev. B* **1996**, *54*, 7830–7836.
- (34) Saito, R.; Tatsumi, Y.; Huang, S.; Ling, X.; Dresselhaus, M. S. Raman Spectroscopy of Transition Metal Dichalcogenides. *Journal of Physics: Condensed Matter* **2016**, *28*, 353002.
- (35) Bernasconi, M.; Marra, G. L.; Benedek, G.; Miglio, L.; Jouanne, M.; Julien, C.; Scagliotti, M.; Balkanski, M. Lattice Dynamics of Layered MPX<sub>3</sub> (M=Mn,Fe,Ni,Zn; X=S,Se) Compounds. *Phys. Rev. B* **1988**, *38*, 12089–12099.
- (36) Kuo, C.-T.; Neumann, M.; Balamurugan, K.; Park, H. J.; Kang, S.; Shiu, H. W.; Kang, J. H.; Hong, B. H.; Han, M.; Noh, T. W. et al. Exfoliation and Raman Spectroscopic Fingerprint of Few-Layer NiPS<sub>3</sub> van der Waals Crystals. *Scientific Reports* **2016**, *6*, 20904.
- (37) Lee, J.-U.; Lee, S.; Ryoo, J. H.; Kang, S.; Kim, T. Y.; Kim, P.; Park, C.-H.; Park, J.-G.; Cheong, H. Ising-Type Magnetic Ordering in Atomically Thin FePS<sub>3</sub>. *Nano Letters* **2016**, *16*, 7433–7438.
- (38) Lloyd, D.; Liu, X.; Christopher, J. W.; Cantley, L.; Wadehra, A.; Kim, B. L.; Goldberg, B. B.; Swan, A. K.; Bunch, J. S. Band Gap Engineering with Ultralarge Biaxial Strains in Suspended Monolayer MoS<sub>2</sub>. *Nano Letters* **2016**, *16*, 5836–5841.
- (39) Mohiuddin, T. M. G.; Lombardo, A.; Nair, R. R.; Bonetti, A.; Savini, G.; Jalil, R.; Bonini, N.; Basko, D. M.; Galiotis, C.; Marzari, N. et al. Uniaxial Strain in Graphene by Raman Spectroscopy: *g*-Peak Splitting, Grüneisen Parameters, and Sample Orientation. *Phys. Rev. B* **2009**, *79*, 205433.

## Graphical TOC Entry

